

A deep *Chandra* observation of the poor cluster AWM 4 – II. The role of the radio jets in enriching the intra–cluster medium.

Ewan O’Sullivan^{*1,2}, Simona Giacintucci^{2,3}, Laurence P. David², Jan M. Vrtilik² and Somak Raychaudhury¹

¹ School of Physics and Astronomy, University of Birmingham, Edgbaston, B15 2TT, UK

² Harvard-Smithsonian Center for Astrophysics, 60 Garden Street, Cambridge, MA 02138

³ INAF – Istituto di Radioastronomia, via Gobetti 101, 40129 Bologna, Italy

Accepted 2010 October 2. Received 2010 September 30; in original form 2010 June 24

ABSTRACT

We use a *Chandra* observation of the poor cluster AWM 4 to map the temperature and abundance of the intra–cluster medium, so as to examine the influence of the central radio galaxy on its environment. While the cluster core is generally enriched to near–solar abundances, we find evidence of super–solar abundances correlated with the radio jets, extending ~ 35 kpc from the core of the central dominant galaxy NGC 6051 along its minor axis. We conclude that the enriched gas has been transported out of the central galaxy through the action of the radio source. We estimate the excess mass of iron in the entrained gas to be $\sim 1.4 \times 10^6 M_{\odot}$, and find that this can be produced in the core of NGC 6051 within the timescale of the AGN outburst. The energy required to transport this gas to its current location is $\sim 4.5 \times 10^{57}$ erg, a significant fraction of the estimated total mechanical energy output of the AGN, though this estimate is dependent on the degree of enrichment of the uplifted gas. The larger near–solar abundance region is also compatible with enrichment by metals mixed outward from NGC 6051 over a much longer timescale.

Key words: galaxies: clusters: general — galaxies: clusters: individual: AWM 4 — galaxies: clusters: intracluster medium — galaxies: active — galaxies: individual (NGC 6051) — X–rays: galaxies: clusters

1 INTRODUCTION

Heating by active galactic nuclei (AGN) is currently regarded as the most likely mechanism preventing excessive cooling of the hot intra–cluster medium (ICM) in galaxy groups and clusters (e.g., McNamara & Nulsen 2007; Peterson & Fabian 2006, and references therein). Cool core clusters typically have a central giant elliptical or cD galaxy, 70–100 per cent. of which host radio sources (Burns 1990; Mittal et al. 2009). Accretion of cooling gas onto the central supermassive black hole of the central galaxy is believed to fuel outbursts which then reheat the cooling material.

Cool core clusters are also known to have strongly centrally peaked abundance profiles (e.g., Böhringer et al. 2004; De Grandi et al. 2004), as are many X–ray bright galaxy groups (e.g., Rasmussen & Ponman 2007). The location of the dominant elliptical at the centre of this peak suggests that it is probably the source of these metals, and observed metal masses are found to be consistent with the quantities expected from supernovae and stellar winds. In particular, the iron mass profiles of systems across a wide range of mass are consistent with long–term enrichment primarily by SNIa

in the central dominant galaxy (Böhringer et al. 2004; Rasmussen & Ponman 2007; Werner et al. 2008).

The iron mass profiles of cool core systems are found to be more extended than the light distribution of the central galaxy, indicating that metals are transported outward from the cluster core (e.g., David & Nulsen 2008; Rasmussen & Ponman 2009). The central AGN is clearly a strong candidate to drive this process, and numerous studies have used metallicity measurements to constrain models of AGN–driven gas motions (e.g., Rebusco et al. 2005, 2006; David & Nulsen 2008; Xiang et al. 2009). Evidence of enrichment associated with the radio jets and lobes of central radio galaxies has been found in nearby X–ray bright clusters (e.g., Sanders et al. 2004; Simionescu et al. 2008, 2009; Kirkpatrick et al. 2009), suggesting that AGN–driven outflows or entrainment is a viable mechanism for transporting enriched gas to large radii. However, with unambiguous examples identified only in a handful of clusters, it is as yet unclear how common this process is, and the identification and characterisation of outflows in other systems is a necessity.

In this paper we construct temperature and abundance maps of the poor cluster AWM 4, so as to investigate the effect of an on–going AGN outburst on the structure of the intracluster medium

* E–mail: ejos@star.sr.bham.ac.uk

(ICM) and in particular the metallicity distribution. The central dominant elliptical galaxy, NGC 6051, hosts a powerful radio source, 4C+24.36, which has been characterised in detail using deep multi-frequency observations from the Giant Metrewave Radio Telescope (Giacintucci et al. 2008). We have previously examined the temperature and abundance structure of the cluster using *XMM-Newton* (O’Sullivan et al. 2005, hereafter referred to as OS05), and the large-scale temperature and abundance profiles of AWM 4 have also been determined from these data (Gastaldello et al. 2008). More recently we have used the *Chandra* data described in this paper to place limits on the properties of the radio galaxy, and in particular to determine the mechanical power required to form the jets and lobes, the nature of the plasma in the lobes, and the properties of the central galactic corona (O’Sullivan et al. 2010, hereafter referred to as paper I).

Both the ICM and galaxy distribution of the cluster appear relaxed, with a concentration of early-type galaxies toward the cluster core (Koranyi & Geller 2002). NGC 6051 shows no indication of having undergone recent interactions (Schombert 1987) and is the most luminous galaxy in the cluster by a significant factor, with a magnitude difference above the second ranked galaxy of $M_{12}=1.6$ (SDSS *g* band). Giacintucci et al. show 4C+24.36 to be a wide-angle-tail radio galaxy with inner jets oriented close to the plane of the sky, probably moving southward with a velocity $\lesssim 120 \text{ km s}^{-1}$. Throughout the paper we assume $H_0=70$, $\Omega_M = 0.3$, and $\Omega_\Lambda = 0.7$. The redshift of the cluster is taken to be 0.0318, and we assume angular size and luminosity distances of $D_A=130.9 \text{ Mpc}$ and $D_L=139.3 \text{ Mpc}$ respectively.

2 OBSERVATIONS AND DATA REDUCTION

AWM 4 was observed by the *Chandra* ACIS instrument during Cycle 9 on 2008 May 18-19 (ObsId 9423), for ~ 80 ks. A summary of the *Chandra* mission and instrumentation can be found in Weiskopf et al. (2002). The S3 CCD was placed at the focus of the telescope and the instrument operated in very faint mode. We reduced the data from the pointing using CIAO 4.1.2 and CALDB 4.1.2 following techniques similar to those described in O’Sullivan et al. (2007) and the *Chandra* analysis threads¹. The level 1 events files were reprocessed, very faint mode filtering applied, bad pixels and events with *ASCA* grades 1, 5 and 7 were removed, and the cosmic ray afterglow correction was applied. The data were corrected to the appropriate gain map, the standard time-dependent gain and charge-transfer inefficiency (CTI) corrections were made, and a background light curve was produced. The final cleaned exposure time was 74.5 ks.

Identification of point sources on S3 was performed using the CIAO task `wavdetect`. Source ellipses were generated with axes of length 4 times the standard deviation of each source distribution. These were then used to exclude sources from all further analysis. A source was detected coincident with the peak of the diffuse X-ray emission; this was not excluded.

Spectra were extracted and responses created for each region following the methods used by the CIAO `specextract` command. Background spectra were drawn from the standard period D set of CTI-corrected ACIS blank sky background events files in the *Chandra* CALDB, normalised to match the 9.5-12.0 keV count rate in the target observation. Very faint mode screening was applied to

the background data. A slight excess of soft emission, compared to the source data, is observed in the background datasets, mainly below 0.5 keV. This is not unexpected, as the soft X-ray background arises largely from hot gas in the Milky Way and from coronal emission associated with solar wind interactions, and is both spatially and temporally variable (e.g., Kuntz & Snowden 2000; Snowden et al. 2004). There are also indications that the spectral shape of the background of the ACIS-S3 CCD has changed since the creation of the period D background files (c.f. the ACIS background cookbook²), which could contribute to the disagreement at low energies. As discussed in paper I, experimentation with fitting different energy bands suggests that ignoring energies below 0.7 keV produces results consistent with those found using *XMM-Newton* in OS05, and these results are relatively insensitive to changes in the absorbing hydrogen column. We therefore ignore counts outside the 0.7-7 keV band in our fits.

We also examined the possibility of modelling the soft background excess, following the technique described by Vikhlinin et al. (2005), in which the background subtracted spectrum of a source-free region is fitted using a zero redshift unabsorbed plasma model with temperature $\sim 0.2 \text{ keV}$, whose normalisation is allowed to be negative. Since AWM 4 entirely fills the S3 CCD, we extracted spectra from the S1 CCD, which is also back illuminated and has a similar response. We ignored energies below 0.5 keV, where instrument calibration is less reliable. We found that a 0.2 keV *apec* model alone, or in combination with a slightly harder 0.3-0.5 keV *apec* model is insufficient to model the residual, owing to a line feature at $\sim 0.55 \text{ keV}$. This probably corresponds to OVII emission, and we therefore added a Gaussian with negative normalisation to model this component. We then tested the effects of this model, appropriately scaled, on fits to spectra from a number of regions on the S3 CCD. The correction was moderately successful, but did not completely remove residuals, suggesting that our model may be too simple or that variations in the background datasets for S1 and S3 are significant. We note that we did not use the combined S1/S3 background file, since this has poorer statistics than the S3-only dataset. The effect of the correction on fit parameters was to marginally raise the temperature and in some regions the abundance, and to increase the uncertainty on all parameters. However, the abundances agreed with those measured in the 0.7-7 keV within the uncertainties, and there was no evidence that the abundance distribution would be altered by using the correction.

Since this analysis was completed, newer blank-sky background datasets (period E), more appropriate for use with this observation, have been released. We have tested the effect of using the period E backgrounds on our results by reprocessing the data, re-extracting the map spectra with the newer background, and re-fitting them. While there are differences in map pixel values, these are within the uncertainties, and we conclude that our original background treatment is sufficient for our goals. Spectral fitting was performed in XSPEC 11.3.2ag. Abundances were measured relative to the abundance ratios of Grevesse & Sauval (1998). We assumed a galactic hydrogen column of $0.05 \times 10^{22} \text{ cm}^{-2}$ (from the FTOOLS task `nh`, based on the data of Kalberla et al. 2005), and 90% uncertainties on fitted parameters were estimated. Spectra were grouped to 20 counts per bin.

¹ <http://asc.harvard.edu/ciao/threads/index.html>

² <http://asc.harvard.edu/contrib/maxim/acisbg/COOKBOOK>

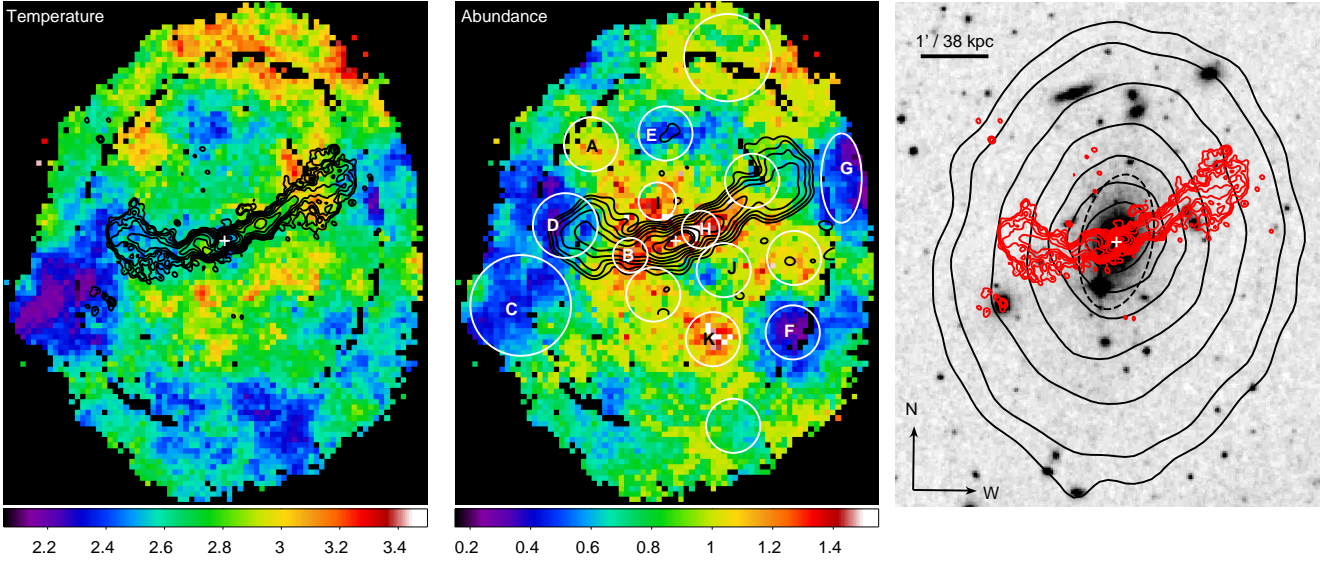


Figure 1. Temperature (*left*) and abundance (*centre*) maps of AWM 4 in units of keV and Z_{\odot} respectively. Black pixels indicate regions with insufficient surface brightness, excluded point sources, or temperature uncertainties exceeding 15%. GMRT 610 MHz contours (starting at 0.2 mJy b^{-1} and spaced by factor 2) are overlaid on the temperature map, 235 MHz contours (starting at 2.4 mJy b^{-1} and spaced by factor 2) on the Abundance map. White crosses indicate the position of the radio core. Circular and elliptical regions on the abundance map were used to compare the maps consistency with normal spectral fits. Lettered regions are discussed in the text. A Digitized Sky Survey B_j -band image (*right*) is shown for comparison, with the same scale and alignment as the other images. The approximate D_{25} contour of NGC 6051 is marked by a dashed ellipse, 610 MHz radio contours are overlaid in red and smoothed X-ray contours (starting at $0.075 \text{ ct. arcsec}^{-1}$, 0.3–2 keV, and spaced by factor $\sqrt{2}$) are overlaid in black.

3 SPECTRAL MAPS

We follow a process similar to that described in OS05 to create adaptively binned 2-D maps of temperature and abundance from the *Chandra* observation. Our mapping technique uses a fixed map pixel size, but allows the spectral extraction region associated with each pixel to vary adaptively. These regions are typically larger than the map pixels, so the resulting pixel values are not independent. The maps are thus analogous to adaptively smoothed images, in which the pixel scale is fixed, but the effective resolution varies over the image. For this reason, we emphasise that we use the maps only as a diagnostic tool, to identify interesting features and regions for further investigation.

We define the map pixels to be square with side length $4.93''$ (10 ACIS physical pixels). We require the associated spectra to contain 1600 net counts in the range 0.7–7.0 keV, extracted using circular regions with radii in the range ~ 14 – $53''$. Spectra were fitted with an absorbed APEC thermal plasma model. Any pixel with an uncertainty in temperature of >15 per cent was excluded as unreliable. The final maps are shown in Figure 1, and an enlarged view of the central part of the temperature map is shown in Figure 2.

Several interesting features are visible in the spectral maps. The central small-scale cool core or galactic corona is visible in the temperature map as a cool region coincident with the centre of NGC 6051 and the origin of the radio jets. There is some indication of cool temperatures along the eastern jet and particularly in the eastern lobe. A weak cavity in the ICM is detected coincident with the eastern lobe (see paper I) and the cool temperatures may arise because of the reduced quantity of high-temperature plasma along the line of sight. The azimuthally averaged temperature profile of AWM 4 declines at radii beyond $\sim 200 \text{ kpc}$ ($\sim 5.25'$), falling to 1.5–2 keV at 400 kpc (Gastaldello et al. 2008), so a cavity in the hot gas will result in a higher fraction of emission from this cool material

in the spectra extracted for this region. In contrast, a hotter region is located where the eastern jet bends sharply north and then returns to its eastward course. The western jet passes through higher temperature regions, particularly where the jet enters the lobe, and the highest temperature material is to the north of the jet at the base of the lobe. High temperatures are also seen in the radio-bright knot in the western jet. Increased temperatures could indicate heating by shocks driven by the jet. Features such as the western knot could indicate obstruction of the jet by ICM plasma, while the correlation with bends in the eastern jet suggests either obstruction or outward motion of the jet “wiggles”. However, the high temperature region in the western lobe is poorly correlated with the radio emission and is likely to be unrelated.

More generally, in the inner part of the cluster temperatures are higher south of the jet than to the north. At larger radii this trend is reversed, with high temperatures in the north and cooler material to the south, east and west. There is no correspondence between the stellar envelope of NGC 6051 and the temperature structure.

The most notable features in the abundance map (Figure 1, middle panel) are a general roughly solar abundance region in the centre of the map, which is asymmetric and clumpy, indicating uneven enrichment of the ICM. Regions of super-solar abundance extend along the jets to the radius of the western knot and the base of the eastern lobe, with some extension to the north. The solar abundance region is somewhat more extended south of the jets, but is less consistent, with patches of both high and low abundance. At larger radii abundances decline, but there is considerable variation, from $\sim 0.4 Z_{\odot}$ regions in the east and west, to solar abundances in the north and south.

The correlation between the super-solar abundance region and the radio jets suggests that enriched material is being entrained outward from the core of NGC 6051. A branch or clump of high abundances also extends north or northeast from the central galaxy. This

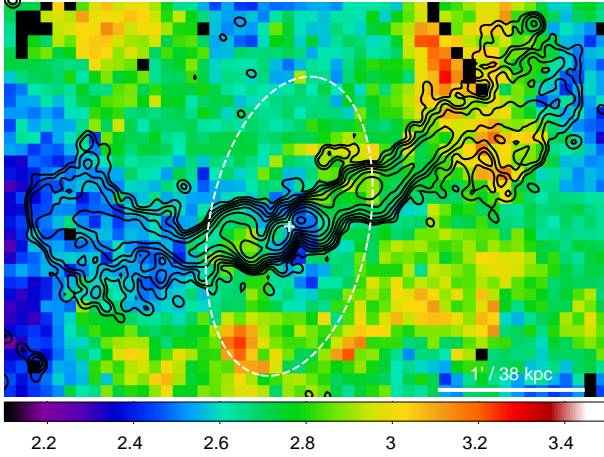


Figure 2. Enlarged view of the temperature map in the region surrounding the radio source. GMRT 610 MHz contours (defined as described in Fig. 1) are marked in black, and the approximate D_{25} contour is marked by a dashed white ellipse. The white cross marks the position of the radio core.

may indicate a trail of material left behind the galaxy, since the bending of the radio jets suggests that NGC 6051 is moving south. Alternatively it could indicate that the entrainment of gas to the east is less closely confined around the jet than is the case on the west. Neither the highest abundance features nor the larger near-solar region correlate with the stellar structure of NGC 6051. The high abundance feature extends roughly across the minor axis of the galaxy, but is more extended than the D_{25} ellipse.

Comparison of the maps with galaxies in the field of view shows no clear correlations. IC 4588, an early-type galaxy at redshift 0.051 falls at the western edge of the large cool, low abundance region to the southeast of the eastern radio lobe (region 1 in Figure 1). It is possible that the cool material is associated with the galaxy, perhaps as part of a galaxy group. Koranyi & Geller (2002) find a small number of galaxies at approximately the same recession velocity. However, there is no clear surface brightness structure in the region, and there are insufficient counts to allow us to identify any additional spectral components. An apparent radio source coincident with IC 4588 is seen in the 610 MHz contours, but comparison with the available GMRT and VLA maps at other frequencies suggests that while there is a source at this position, its apparent extension is the result of a noise feature.

3.1 Metal enrichment along the jets

Figure 4 shows the map of best-fitting abundance values and the associated 90 per cent upper and lower bound maps. The central abundance feature which correlates with the jets is clear in all three maps. Maps of the fit statistic show variation across the field, but do not appear correlated with the temperature or abundance maps. This suggests that the apparent features are not the product of poor spectral fits in particular regions. We test this conclusion more thoroughly in Section 3.2.

To examine the high abundances associated with the radio jets, we placed a number of rectangular regions along and across the jet, shown in Figure 3. Smaller regions are used in the inner part of the jet to allow us to look for any central abundance peak, larger regions outside to minimise the uncertainties on abundance. Spectra were extracted from these regions and fitted with an absorbed

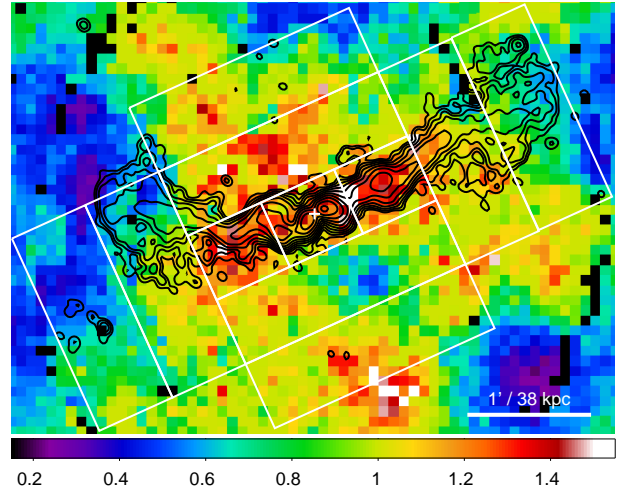


Figure 3. Abundance map of the core of AWM 4, with GMRT 610 MHz contours overlaid. Rectangular regions were used to examine the variation in abundance across and along the jet. The white cross marks the position of the radio core.

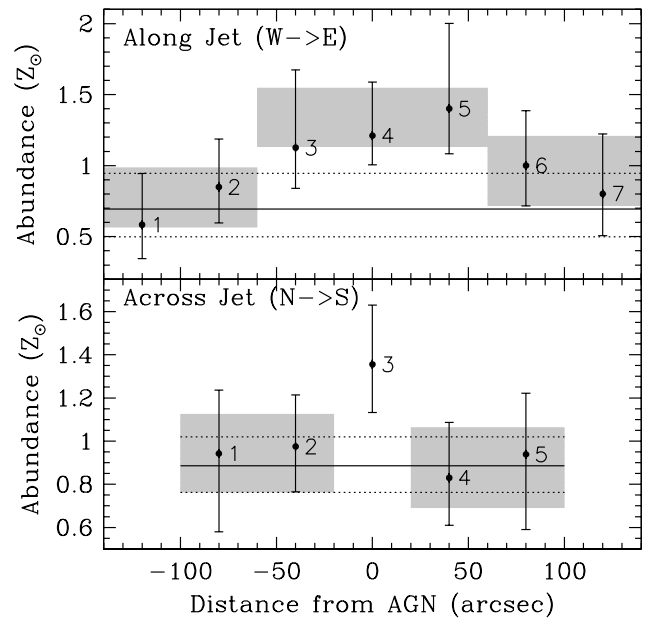


Figure 5. Measured abundances in profiles running east to west along the radio jets and north to south across the jets, using the regions shown in Figure 3. Black points with error bars indicate measurements in individual bins with 90% uncertainties. Numerals beside each point indicate the bin numbers referred to in the text. Grey boxes show the uncertainty region when adjacent bins are fitted simultaneously. Black solid lines represent the combined best fit to spectra 1 and 7 on the E-W profile, and 1, 2, 4 and 5 on the N-S profile, with 90% uncertainties shown by dotted lines.

APEC model. The resulting abundances are shown in Figure 5. The east to west profile uses the two large rectangular regions at each end, and the smaller rectangles along the jet; the north to south profile compares the upper and lower pairs of large rectangular regions, and the central region comprising the three small rectangles combined.

While the abundances in neighbouring regions are compara-

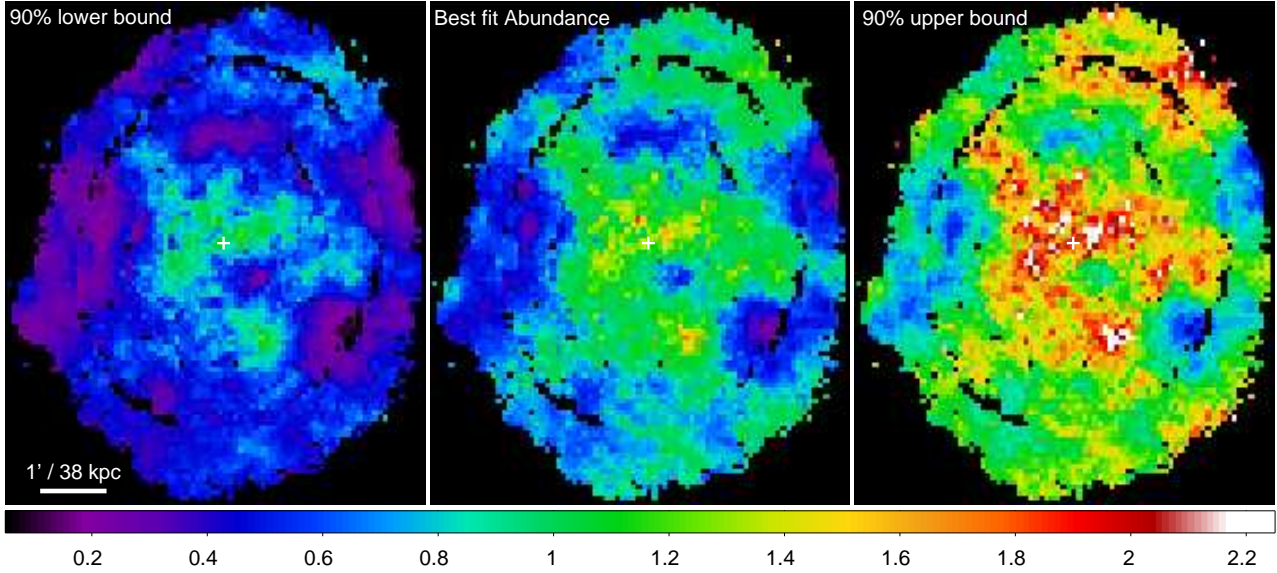


Figure 4. Abundance maps of AWM 4 in solar units, showing (*centre*) the best-fitting value and the 90% lower (*left*) and upper (*right*) bounds. Abundances are in solar units. Note that the best-fit abundance map is the same as that shown in Figure 1, but that the colour scale has been selected to allow direct comparison with the uncertainty maps. White crosses mark the position of the radio core.

ble, there is a clear trend for higher abundances in the inner jets (the three central regions of the east–west profile) and declining abundance outside that area. The abundance of the westernmost region is lower than the abundances in the inner jet at 90% significance. Combining regions of similar metallicity, we find that the inner part of the jets (regions 3–5 of the E–W profile, or region 3 of the N–S) is more enriched than the regions at the eastern end of the jet at 3.2σ significance, but only at a 2.0σ level in comparison to the western regions. However, comparing the inner jet to a combination of the extreme western and eastern regions shows a 3.4σ difference. The northern and southern regions, combined in pairs, are less abundant at the 2.4 – 2.7σ level, or 3σ if all four are simultaneously fitted. In general, we conclude that the high abundance region is more extended E–W than N–S, following the jet, and that its abundance is significantly greater than its surroundings, by $\sim 0.4Z_{\odot}$.

3.2 Accuracy of the spectral maps and potential sources of bias

To test the accuracy of the maps we defined regions covering specific temperature and abundance features, extracted spectra from these regions, and fitted them. The regions contain between ~ 660 and ~ 2900 net counts in the 0.7–7.0 keV band. While the spectral extraction and fitting process is identical in mapping and normal spectral analysis, these regions were not constrained to contain a fixed number of counts, so should provide a test of the smoothing-like effect of the mapping process. It also allows us to determine how well the variation within map regions corresponds to the uncertainty on the normal spectral fit. Figure 6 shows comparisons of the range of temperatures and abundances found in the map regions with the values derived from the spectral fits.

In general the maps appear to provide an accurate estimate of both temperature and abundance. One spectral fit, for region A, finds a significantly higher temperature than the map suggests. This appears to be a smoothing issue, the spectral extraction regions used to create the map being significantly larger than re-

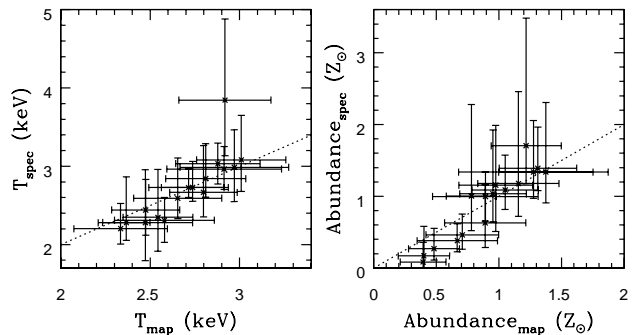


Figure 6. Comparison of temperatures and abundances derived from the spectral maps and from normal spectral fitting for the numbered regions shown in Figure 1. Error bars indicate the 90% uncertainty on the parameter from the spectral fits, or the range of parameter values found in the region in the “best-fit” spectral maps. Dotted lines indicate agreement between the two methods.

gion A, which contains only ~ 900 net counts (0.7–7.0 keV). The abundance measurements typically have larger uncertainties, and a greater variation in map pixel values, particularly in the highest abundance regions. The highest abundance of any spectral fit is found in region B. The region contains ~ 1200 net counts, again suggesting that smoothing lowers the maps values, but the spectral fit agrees with the map within the uncertainties. The regions with lowest abundances (regions C,D,E,F and G) appear to have map values which are slightly overestimated. However, they are again consistent within the uncertainties.

The abundances measured in the map spectral fits could be biased by a number of issues which arise from the assumption of a simple single temperature plasma model when fitting spectra which must, on some level, be produced by gas whose properties vary within the spectral extraction region. One possible problem is the inverse Fe-bias (Rasia et al. 2008; Simionescu et al. 2009;

Gastaldello et al. 2010), which can affect abundance measurements made using single temperature models fitted to gas with a mean temperature of 2–4 keV. If the gas has a complex, multi-temperature structure, abundance may be overestimated owing either to the mixture of differing levels of Fe-L and Fe-K shell emission along the line of sight (Rasia et al. 2008), or the behaviour of the spectral fitting code when a single temperature model is used to describe a multi-temperature spectrum (Gastaldello et al. 2010).

Testing for this type of problem is difficult, in that high signal-to-noise spectra are required if multi-temperature models are to be fitted successfully, but larger regions are more likely to contain significant temperature variations. To determine whether the inverse Fe-bias is likely to affect our abundance measurements, we performed three tests:

(i) We combined regions 3–5 of the E–W profile described in Section 3.1 and fit a two-temperature plasma model to the 0.7–7 keV band, with the two abundances tied. The model converges on temperatures of ~ 2.6 keV for both components, but neither temperature or normalisation are constrained, indicating that either component can fit the data adequately without need for a significant contribution from the other. The abundance is found to be $1.33^{+0.22}_{-0.20} Z_{\odot}$, in good agreement with the single temperature fit. The gas thus appears to be close to single-temperature in this region.

(ii) Using the same combined spectra from regions 3–5, we fitted single-temperature models separately to the 0.7–2 keV and 2–7 keV bands. Table 1 shows the results of these fits. The hard band fit finds a somewhat lower abundance, while the soft band fit finds higher abundance and temperature. However, the uncertainties are large and both abundances are consistent with the broad-band best-fitting value and with each other at the 90 per cent level.

(iii) We recreated the spectral maps using $\sim 10''$ pixels, requiring 3200 counts per spectrum, and allowing spectral extraction regions of radius 19–74''. The spectra were fitted using a two-temperature APEC model with abundance tied between the two components. These fits were successful for ~ 50 per cent. of the spectra, with a single component dominating in the remainder. The regions in which the two-temperature model produces a useful fit are not correlated with the X-ray or radio surface brightness, or with the temperature or abundance structures. The resulting abundance map shows the same structure as our main abundance map, and the differences in abundance between the two maps are not correlated with any particular regions, i.e. we see no evidence of a systematic over- or under-estimation of abundance along the radio jets. There is no indication that those pixels with a significant contribution to the spectrum by the second temperature component have higher or lower abundances in the two-temperature fits. The only region near the radio source in which we see both a high abundance and evidence that a two-temperature model is a reasonable fit to the data is in the knot of the western radio jet (roughly corresponding to region H on Figure 1). Spectra from pixels in the two highest abundance regions outside the jets (regions I and K) appear to be best modelled as single-component spectra, as do some of the lowest abundance pixels (region C). The low abundance clump just south of the jet, in the east of region J, includes a mix of pixels whose spectra produce useful two-temperature fits and those which are best fit with single temperature models. In general we conclude that there is no evidence that the abundance distribution would be significantly altered by the use of two-temperature fits.

A powerlaw emission component associated with the radio jets or lobes could also affect the measured abundance. If the pow-

Energy band	kT (keV)	Abundance (Z_{\odot})	red. χ^2	d.o.f.
0.7–7.0	$2.66^{+0.10}_{-0.09}$	$1.32^{+0.23}_{-0.19}$	0.926	327
0.7–2.0	$2.92^{+0.34}_{-0.29}$	$1.63^{+0.54}_{-0.37}$	0.941	215
2.0–7.0	$2.72^{+0.24}_{-0.22}$	$1.08^{+0.51}_{-0.43}$	0.848	104

Table 1. Spectral fits to the broad band emission from the region along the radio jets, compared with fits to soft and hard sub-bands.

erlaw slope is similar to that of the bremsstrahlung continuum, fitting the spectrum with a simple plasma model is likely to result in an underestimate of abundance. If the powerlaw provides more emission at higher energies, the plasma model temperature is likely to be biased high, and abundances overestimated. The expected flux from inverse Compton scattering in the radio lobes is too low to be detected, and indeed no evidence powerlaw emission is found (see paper I). To test whether there could be significant powerlaw emission from the jets, we fit apec+powerlaw models to the spectra extracted in the E–W and N–S profiles. If a powerlaw component were associated with the jets we would expect to see the highest fluxes from regions 3–5 of the E–W profile, and none in regions 1, 4 and 5 of the N–S profile. In practise we find powerlaw contributions to be consistent with zero in all regions except regions 2 and 3 of the E–W profile, and region 1 of the N–S profile. In these regions the best-fitting powerlaw index is inverted, and the component only produces significant additional flux above 5 keV. If the powerlaw index is fixed at $\Gamma=2$, as expected from the radio spectral index (see paper I), the powerlaw flux is consistent with zero. We therefore conclude that no significant powerlaw emission is detected from the jet, and that the abundances are not biased in this way.

High abundances could also be found in error if the plasma is not in ionisation equilibrium. Kaastra et al. (2009) point out that the Maxwellian electron distribution assumed for thermal plasmas is not valid in shocked regions. Non-thermal electrons alter the X-ray spectrum and can lead to the overestimation of the abundance; A possible example is seen in the high abundance arc associated with the shock in HCG 62 (Gitti et al. 2010). Both shocks or mixing of non-thermal electrons into the thermal plasma could occur along the edge of the radio jets in AWM 4. The weak surface brightness features associated with the jets could indicate the presence of compressed gas (see paper I, fig. 2). However, we might expect that shocks capable of affecting the abundance measurements would be detectable as either density or temperature features. The only regions where such features may be visible are in the western knot and eastern bend of the jets, but our data are insufficiently deep to confirm or reject this.

We also note that we might expect to find both mixing of relativistic electrons from the radio source and multi-phase gas in the lobes of the radio source as well as the jets, since the lobes appear to contain a mix of thermal and relativistic plasmas (see paper I). The lack of high abundances coincident with the lobes therefore argues against these sources of bias being effective. The small extension of the high abundance region north of the galaxy core also cannot be explained as a shock or jet-related feature.

We therefore conclude that while it is likely that the spectra used in the maps do contain emission from multiple plasma components with different temperatures and abundances, the variation is probably not large enough to affect our results, and the single-temperature fits provide a sufficiently accurate estimate of abundance for our purposes.

3.3 Comparison with XMM-Newton spectral maps

Comparison of the *Chandra* spectral maps with the *XMM-Newton* maps of OS05 reveals some differences, particularly in the abundance distribution. The *XMM-Newton* abundance map contains a ridge of high metallicity extending from the galaxy core northwest along the northern edge of the western jet. Testing with normal spectral fits to the *XMM-Newton* data confirmed that this region had enhanced abundances, ruling out a problem specific to the mapping technique. OS05 suggested that the feature might arise from stripped material or a shock associated with the jet. The *Chandra* data show no such ridge, though high abundances are seen in the galaxy core.

To confirm the lack of such a feature in the *Chandra* data we extracted a spectrum in an annular segment defined from the *XMM* abundance map, extending northwest, from $\sim 45\text{--}120''$ from the AGN, equivalent to region 1 of Figure 9 and Table 5 of OS05. This spectrum, and the *XMM* spectra extracted from region 1 by OS05 using SAS 6.0, were then fitted with an absorbed APEC model using a range of energy bands.

We find that 1) although *Chandra* ACIS and *XMM* EPIC-pn and MOS cameras give consistent abundances within the errors, the EPIC-pn spectra produce the highest best-fit abundances and ACIS the lowest, and 2) the abundance measured is affected by the energy band used, with wider energy bands producing higher abundances in this region. Using our 0.7–7.0 keV energy band, EPIC-MOS produces best-fit abundances very similar to ACIS ($0.78^{+0.39}_{-0.28}$ compared to $0.70^{+0.17}_{-0.15} Z_{\odot}$) while the EPIC-pn abundance is significantly greater ($1.01^{+0.28}_{-0.24}$). This suggests that *XMM* map feature is either the product of inaccurate calibration of the EPIC-pn, or that it is caused by the presence of some spectrally hard emission component which affects the EPIC-pn more than ACIS or EPIC-MOS because of its greater effective area at high energies.

As discussed in OS05, the high abundance ridge does not correspond to detector structure on either EPIC-MOS or -pn. The ridge is located on the focal-point CCD of EPIC-pn, at least $45''$ northwest of the CCD edge at the centre of the array. There are no structures in the background data files at the position of the ridge. It therefore seems unlikely that a calibration problem associated with a particular CCD feature could be the cause of the high abundances.

Examining hard band images (5–7 keV) some clumps of emission are visible, but these are not consistent between instruments and involve only a handful of counts. Unfortunately neither dataset is sufficiently deep to determine whether an excess is present. Fitting the MOS and pn spectra described above using an apec+powerlaw model, we find neither can constrain the power-law index, and that for various fixed index values the MOS abundance is still consistently lower than that measured for the EPIC-pn. This argues against an additional spectral component as the cause of the ridge, and leaves the origin of the feature uncertain. To check whether any hard emission affects our *Chandra* maps we recreated the maps using 3200 count spectra, and ignoring energies above 3.0 keV. We find that the map structures do not change, suggesting that our results are not affected by extraneous hard emission.

4 DISCUSSION

While we have focussed on the interaction between the AGN and ICM, there are other mechanisms which could affect the abundance and temperature structure of AWM 4. Gas motions associated with mergers and interactions are one possibility. The overall structure

of the temperature map, with higher temperatures to the south of the radio jet than to its north at moderate radii, with the pattern reversed at large radii, could in principle be an indication of gas sloshing. The infall of a subcluster can disturb the gravitational potential of the cluster, causing the cluster core to oscillate around its centre, sloshing the gas of the core back and forth. Examples of gas sloshing have been documented in a number of clusters (e.g., Markevitch et al. 2001; Mazzotta & Giacintucci 2008; Simionescu et al. 2010), and confirm the results of numerical simulations (e.g., Ascasibar & Markevitch 2006), in that the sloshing is observed to produce a spiral pattern of cold fronts, where cool gas from the cluster core is moved outward and brought into contact with hotter material. The staggered pattern of temperature reversals seen to north and south of the radio source could be produced by such spiral sloshing. The apparent southward motion of NGC 6051 could also be explained if the cluster core is in motion relative to its surroundings. Sloshing provides a mechanism for transporting metals out of the cores of clusters (Simionescu et al. 2010), and would therefore be relevant to our study of AWM 4.

However, there are several strong arguments against sloshing being important in this cluster:

- No cold fronts or sharp changes in surface brightness are detected anywhere in AWM 4, and there is no evidence of surface brightness features corresponding to the temperature structure. There is evidence that the surface brightness is generally greater north of the radio source than to the south, but this appears to be caused by a mild offset between the position of NGC 6051 and the centroid of the ICM emission. In general the surface brightness suggests that the ICM is relaxed.
- There is no obvious candidate for the subcluster needed to set the sloshing in motion. No substructure is observed in the X-ray, no galaxies of comparable luminosity to NGC 6051 are observed in the system, and there is no evidence of substructure in the galaxy spatial or velocity distribution (Koranyi & Geller 2002).
- If sloshing has occurred, we would expect correlation between temperature and abundance structure. Instead, we find NGC 6051 located near the centre of the inner, near-solar abundance region, with high abundances correlated with low temperatures north of the radio jet, but with high temperatures south of the jet.

We therefore conclude that while NGC 6051 may be in motion, it is unlikely that large-scale gas sloshing is occurring in AWM 4.

4.1 Metal mass and energetics

Under the assumption that iron is the dominant element determining the measured metallicities, we can estimate the mass of iron required to produce the raised abundance seen along the jets,

$$m_{Fe} = \rho V \Delta Z \gamma_{Fe}, \quad (1)$$

where ρ is the density of the gas in the jets, V is the volume of the region, ΔZ is the excess abundance above the background enrichment level and γ_{Fe} is the solar iron mass fraction (1.28×10^{-3} for the abundances of Grevesse & Sauval 1998). For this purpose, we define the volume of high enrichment along the jets using the smallest rectangular regions in Fig. 3 and assuming a rotational symmetry around the jet axis, to produce three cylinders of radius 11 kpc and length 20 kpc. Gas densities in each cylinder are taken to be the average density at the mean radius of the region, as determined in paper I. We take the abundance of this region to be $1.3 Z_{\odot}$, based on the mean value found for the regions

along the jet. The abundances measured from the rectangular regions around the jet suggest a background level of $0.9Z_{\odot}$, but the clumpiness of the abundance distribution on these scales makes this uncertain. To get a more reliable measure of the general level of enrichment in the central part of the cluster, we extracted a spectrum from a circular region of radius $\sim 100''$ (~ 65 kpc) centred just south of the radio core, with the region of the jets excluded. This encloses the whole high abundance part of the cluster core, and while there is spatial variation in metallicity, it should provide a reasonable average enrichment level. The best fitting abundance for this region is $0.86_{-0.08}^{+0.09}Z_{\odot}$, suggesting that a background abundance of $0.9Z_{\odot}$ is acceptable. This then suggests an excess iron mass of $\sim 1.4 \times 10^6 M_{\odot}$.

Beyond the $0.9Z_{\odot}$ central region the mean abundance falls to $\sim 0.6Z_{\odot}$. From the gas mass profile of OS05, we estimate the total gas mass within 65 kpc to be $6.3 \times 10^{10} M_{\odot}$. For an excess abundance of $0.3Z_{\odot}$, this suggests that the volume has been enriched by an additional $2.4 \times 10^7 M_{\odot}$ of iron.

NGC 6051 is the most massive galaxy in AWM 4 by a significant margin, and given its central position it is likely to be the source of a large fraction of the enrichment. If the super-solar abundances are associated with material entrained by the radio jets, the gas now seen along the jets must have been enriched in the galaxy core. Using the regions described above, we can estimate that if the enriched material was originally all in the central ~ 10 kpc of the galaxy, $\sim 45\%$ of the metals originally formed in this central region have been transported out along the jets.

We can assume that the emission observed from the region of the jets represents a mix of gas, both highly enriched uplifted material and the lower metallicity gas which occupied the whole region. The two phases may be physically mixed or separate, but the measured abundance represents an average of the two. The mass of enriched gas which must be uplifted and the energy required to do so will depend on the level of enrichment and on the abundance of the gas it mixes with. If the core were very highly enriched, even a small amount of gas transported outward would produce the abundances we observe, when mixed with the less enriched gas at that radius. We can define the mass of gas which must be transported to be:

$$m_{trans.} = \frac{Z_{obs} - Z_{prior}}{Z_{enrich} - Z_{prior}} \rho V, \quad (2)$$

where $\rho V = m_{gas} = 1.19 \times 10^9 M_{\odot}$ is the mass of gas in the jets outside the core, Z_{obs} is the abundance now observed in the jets, Z_{prior} is the abundance in the jets prior to mixing with more enriched material from the core, and Z_{enrich} is the abundance of that highly enriched material. If we assume that the jets expanded into material with abundance $Z_{prior} = 0.9Z_{\odot}$, as for the surrounding gas, we can estimate Z_{enrich} by assuming that the excess metals now observed in the jets were once in the core. This suggests that the uplifted enriched material had an abundance $Z_{enrich} = 1.6Z_{\odot}$. In this case $m_{trans.} = 0.57 \times m_{gas}$. The energy required to uplift the gas from the core is simply the change in gravitational potential energy as the gas is lifted from the core to the mean radius R , $E = GM_{tot}(< R)m_{trans.}/R$ where $R \sim 20$ kpc, $M_{tot}(< R) = 1.54 \times 10^{12} M_{\odot}$ is the total mass within this radius (from OS05), and G is the gravitational constant. For $m_{trans.} = 0.57 \times m_{gas}$, this gives $E = 4.5 \times 10^{57}$ erg. The maximum energy which could be required ($E = 7.9 \times 10^{57}$ erg) corresponds to the case where the gas uplifted has $Z_{enrich} = Z_{obs}$, in which case all the gas currently in the jets has been uplifted, displacing that which was there prior to the outburst. Less energy will

be required if higher enrichment levels are assumed in the core; taking the 90 per cent. upper bound on the current abundance there ($1.6Z_{\odot}$) and again assuming the excess metals in the jets originated in the core, its abundance would have been $\sim 1.9Z_{\odot}$, giving $m_{trans.} = 0.4 \times m_{gas}$ and uplift energy $E = 3.2 \times 10^{57}$ erg. In any case, the energy required to uplift the enriched material is a significant fraction of the expected mechanical power output of the jets, which we estimate to be $9.4 \times 10^{58} \phi$ erg, where ϕ is the filling factor of the lobes (see paper I). Our best estimate of filling factor, for the western lobe where a cavity is detected, is $\phi = 0.21$, and the 3σ upper limit on the mean filling factor of the two lobes is $\phi < 0.6$. This suggests that >20 per cent. of the mechanical energy of the jets could be required to produce the observed uplift.

Further limits on the level of enrichment of uplifted material can be estimated based on surface brightness. If we assume that the pressure of the uplifted material decreases as the gas rises, maintaining pressure equilibrium with its surroundings, we can consider two extreme cases; either the pressure decrease is achieved through density decrease (expansion) or through temperature decrease. For each case, we can estimate the expected surface brightness increase for a given abundance and mass of uplifted gas (Z_{enrich} and $m_{trans.}$).

As discussed in paper I, there is some apparent increase in surface brightness along the jets, but these features are not statistically significant. Determining a ‘background’ level of surface brightness is also difficult, since the mild offset between the position of NGC 6051 and the X-ray centroid of the ICM means that surface brightness north of the jets is systematically brighter than to the south, and there is some evidence of additional structures north of the jet. We determine the 0.7–3 keV surface brightness in a number of segments of an elliptical annulus chosen to match the mean ellipticity of the diffuse emission, corrected using a 1.05 keV monoenergetic exposure map. As expected, surface brightness declines from north to south across each jet by a factor larger than the statistical uncertainty, and there is significant bin-to-bin variation around the annulus, beyond that expected for a smooth distribution. For excess surface brightness to be detected in the jets, it would have to exceed that of the brighter neighbouring bin by a significant margin. We define this as an increase of three times the mean variation between bins across the jets.

On this basis, we can consider two possible scenarios, depending on whether the uplifted material expands adiabatically or isothermally as it rises. The first case would occur if conduction between the material and its surroundings is strongly suppressed, the latter if conduction were highly efficient. For adiabatic expansion, we can determine the expected change in temperature for a monatomic ideal gas using the relation $T_2 = T_1 (P_2/P_1)^{(\gamma-1)/\gamma}$, where T and P are temperature and pressure before (1) and after (2) expansion, and the adiabatic index $\gamma = 5/3$. The known change in pressure then allows us to calculate the expected change in density. We find that the uplifted material would still be both cooler and denser than the surrounding gas, and therefore significantly more luminous than the surrounding ICM with even $1.3Z_{\odot}$ abundance. The surface brightness limit for the west jet rules out this scenario. For the east jet, the upper limit on surface brightness suggests limits on the uplifted material of $Z_{enrich} \lesssim 1.4Z_{\odot}$ and $m_{trans.} \lesssim 0.8 \times m_{gas}$. For the second case, in which the uplifted gas expands isothermally as it rises, we estimate limits of $Z_{enrich} \lesssim 2Z_{\odot}$ and $m_{trans.} \lesssim 0.36$ in the western jet, and $Z_{enrich} \lesssim 1.7Z_{\odot}$ and $m_{trans.} \lesssim 0.5$ in the eastern jet. In practice, this suggests that the gas mainly expands as it rises, with only slight cooling. These limits ignore the possible presence of channels or

sub-cavities from which ICM plasma has been excluded by the jets, which would reduce surface brightness. Nonetheless, we conclude that our initial estimate of the mass of uplifted gas and the energy required to transport it are probably correct.

We can estimate the timescale over which these levels of enrichment might occur using the relation of Böhringer et al. (2004),

$$t_{enr} = (10^{-12} S \nu_{Fe} + 1.5 \times 10^{-11} t_{15}^{-1.3} Z_* \gamma_{Fe})^{-1} \frac{M_{Fe}}{L_B / L_{B\odot}}, \quad (3)$$

where t_{enr} is the timescale required to produce the iron, S is the supernova rate (we assume 0.18 SNU or ~ 0.0125 SN yr $^{-1}$ for NGC 6051, from Cappellaro et al. 1999), Z_* is the stellar metallicity, $\nu_{Fe}=0.7M_{\odot}$ is the iron yield from SNIa (Nomoto et al. 1997, for the WDD2 model) and γ_{Fe} is the iron mass fraction in stellar mass loss. The rate of stellar mass loss is derived from the approximation $\dot{M} = 1.5 \times 10^{-11} t_{15}^{-1.3} L_B / L_{B\odot}$ for a passively evolving old stellar population (Ciotti et al. 1991), where t_{15} is the age of the stellar population as a fraction of 15 Gyr. Neither the age or mean abundance of the stellar population of NGC 6051 have been measured, and we therefore assume an age of 10 Gyr (equivalent to all stars forming at a redshift ~ 2) and an abundance of $1.6Z_{\odot}$ (comparable to similar ellipticals, Denicoló et al. 2005). On this basis, enrichment of the $\sim 0.9Z_{\odot}$ region from a starting abundance of $0.6Z_{\odot}$ would require ~ 1.9 Gyr. Unsurprisingly, this is far longer than the estimated timescale of the current AGN outburst (~ 170 Myr, Giacintucci et al. 2008, paper I). We would expect metals in the inner part of the cluster to have built up over the whole lifespan of the system, and while we are treating this as a plateau level of enrichment, it is consistent with the broad abundance peak seen in most galaxy clusters (see paper I for a radial abundance profile). However, this estimate suggests that it is at least plausible that NGC 6051 has provided most or all of the enrichment in this region.

The mass of iron required to enrich the gas along the jet from 0.9 to $1.3Z_{\odot}$ could be produced in 107 Myr, well within the outburst timescale. Since the enrichment of the $\sim 1.3Z_{\odot}$ gas is occurring in a reduced volume at the core of the galaxy, this timescale is probably underestimated, but considering that the stellar density is highest in this region it seems reasonable to expect that enrichment by stellar processes is capable of producing the high abundances observed along the jet.

The location of the enriched gas along the jets rather than in the lobes provides some information about the method by which the gas is transported. In the nearby radio galaxy Centaurus A, it has been suggested that material can be directly entrained from stars located within radio jets (Nulsen et al. 2010). While this provides a natural route for increasing the mass loading of jets to the levels required to provide pressure equilibrium between radio lobes and their environment (see paper I for discussion of this possibility in AWM 4), it is unlikely to provide the abundance structures we observe. We would expect material entrained within the jets themselves to be rapidly transported into the lobes, and probably to have a high temperature and low density, precluding detectable X-ray emission in the energy band which we have observed.

The more likely alternative is that the enriched gas is being uplifted more slowly by gas motions associated with the growth of the radio jets and lobes. Numerical modelling of AGN jet/gas interactions suggest that the buoyant rise of cavities associated with radio lobes causes subsonic gas motions, drawing gas out of the cluster core along the line of the jets (e.g., Brüggén 2002; Roediger et al. 2007). In this scenario, the enriched material occupies a volume around the jets, where gas motions produce an overall outward motion similar to the growth velocity of the radio source, but with-

out being accelerated by interaction with the relativistic jet plasma. The lack of shocks associated with the lobes of 4C+24.26 indicates that they are moving subsonically, and the buoyant timescale (~ 130 Myr, paper I) is comparable to the radiative age of the lobes. It is therefore likely that the lobes have risen buoyantly to their current position, uplifting enriched gas behind them.

4.2 Other sources of enrichment

In principle, metals could be produced along the jets through local star formation, perhaps caused by compression of cool material by the jets. Assuming that our mean metallicity measurements are determined largely by the iron abundance, we can estimate that $\sim 2 \times 10^7$ SNII would be needed to enrich the gas to $1.3Z_{\odot}$, assuming an initial $0.9Z_{\odot}$ abundance. With a simple assumption of one supernova per $100M_{\odot}$ of stars formed, this is equivalent to a star formation rate (SFR) of $\sim 12 M_{\odot} \text{ yr}^{-1}$ over the 170 Myr timescale of the AGN outburst.

Assuming a 10% efficiency rate for the star formation, we require $2 \times 10^{10} M_{\odot}$ of cool gas to have been present along the jets, and presumably larger masses in the galaxy as a whole. This is comparable to the mass of the hot ICM within a radius equal to the extent of the radio source ($\sim 6 \times 10^{10} M_{\odot}$, OS05). Cool gas and star formation is detected in some clusters (e.g., Edge & Frayer 2003; Salomé & Combes 2003; Bildfell et al. 2008; Pipino et al. 2009), but is typically associated with large cool cores or mergers. The estimated SFR is comparable to those observed in some massive cooling flow clusters (O’Dea et al. 2008) and large compared to rates found from UV observations of less extreme systems (Hicks et al. 2010). If the enrichment is produced by SNII, we would expect to see a clear change in abundance ratios between regions inside and outside the jet, and probably considerably higher abundances of Si than Fe. We fitted vapec models to the spectra from the regions shown in Figure 3, leaving Fe and Si free to vary. The resulting abundances are in many cases not very tightly constrained, but we generally find abundance ratios Si/Fe ~ 1 , with uncertainties of a factor of 2. These uncertainties are large enough to render estimates of the numbers of supernovae of different types necessary to enrich the gas impractical, but there is no systematic change in the ratio outside the jets, suggesting that the gas throughout the core has probably been enriched by a similar mix of SNIa and SNII. The alignment of the enriched region along the jet, and its extent well beyond both the central corona and the optical body of the galaxy, is also difficult to explain through star formation fuelled by cooling or gas brought into NGC 6051 by a merger. We might also expect the $\sim 2 \times 10^9 M_{\odot}$ of young stars formed within the lifetime of the jet to be detectable, as a significant fraction would form at large radii along the galaxy minor axis. It therefore appears unlikely that the high abundances observed in the jet are the product of recent star formation.

5 SUMMARY

Temperature and abundance maps of the poor cluster AWM 4 reveal a high degree of structure in this relatively relaxed poor cluster. Features in both temperature and abundance are found to correlate with the jets of the central radio source, with a cool region corresponding to the eastern lobe and cavity, and supersolar abundances extending from the galaxy core along both jets. Testing against normal spectral analysis, and variation of the number of counts and

energy band used in the map spectral fits shows the maps to be reliable, and we conclude that the features correspond to real physical structures within the ICM.

The location of high abundances along the jets suggests that material enriched in the inner parts of NGC 6051 has been entrained and is being transported out of the galaxy, roughly along its minor axis. The mass of iron required to produce such a feature ($\sim 1.4 \times 10^6 M_{\odot}$, assuming enrichment by $0.4Z_{\odot}$) is relatively modest, and it is likely that it could be produced in the central region of NGC 6051 on a timescale comparable to that estimated for the AGN outburst. The energy required to transport the gas to its observed location is $\sim 3 - 8 \times 10^{57}$ erg, depending on the abundance of the uplifted material and the gas it mixes with. This is a significant fraction of the estimated total energy required to inflate the lobes of the radio source. An extended region of near-solar abundances which extends out to ~ 65 kpc in the ICM is also likely a product of enrichment by the central galaxy, though over timescales much longer than the AGN outburst. Galaxy motions and previous AGN outbursts may have contributed to transporting metals into this region.

While it is possible that some degree of bias affects the abundance measurements, arising either from the complex temperature structure of the ICM or from non-thermal electron populations associated with the jets, neither possibility seems able to explain the observed abundance structures. We therefore conclude that AWM 4 is one of the growing number of systems in which evidence is seen for enrichment of the ICM via entrainment of high-abundance gas by radio jets.

Acknowledgements

The authors thank the anonymous referee for a number of comments which have materially improved the paper. Support for this work was provided by the National Aeronautics and Space Administration through Chandra Award Number GO8-9127X-R issued by the Chandra X-ray Observatory Center, which is operated by the Smithsonian Astrophysical Observatory for and on behalf of NASA under contract NAS8-03060. E. O'Sullivan acknowledges the support of the European Community under the Marie Curie Research Training Network. We thank the staff of the GMRT for their help during the observations. GMRT is run by the National Centre for Radio Astrophysics of the Tata Institute of fundamental Research. We acknowledge the usage of the HyperLeda database (<http://leda.univ-lyon1.fr>).

REFERENCES

- Ascasibar Y., Markevitch M., 2006, *ApJ*, 650, 102
 Böhringer H., Matsushita K., Churazov E., Finoguenov A., Ikebe Y., 2004, *A&A*, 416, L21
 Bildfell C., Hoekstra H., Babul A., Mahdavi A., 2008, *MNRAS*, 389, 1637
 Brüggén M., 2002, *ApJ*, 571, L13
 Burns J. O., 1990, *AJ*, 99, 14
 Cappellaro E., Evans R., Turatto M., 1999, *A&A*, 351, 459
 Ciotti L., D'Ercole A., Pelegrini S., Renzini A., 1991, *ApJ*, 376, 380
 David L. P., Nulsen P. E. J., 2008, *ApJ*, 689, 837
 De Grandi S., Ettori S., Longhetti M., Molendi S., 2004, *A&A*, 419, 7
 Denicoló G., Terlevich R., Terlevich E., Forbes D. A., Terlevich A., Carrasco L., 2005, *MNRAS*, 356, 1440
 Edge A. C., Frayer D. T., 2003, *ApJ*, 594, L13
 Gastaldello F., Buote D. A., Brighenti F., Mathews W. G., 2008, *ApJ*, 673, L17
 Gastaldello F., Ettori S., Balestra I., Brighenti F., Buote D. A., De Grandi S., Ghizzardi S., Gitti M., Tozzi P., 2010, [arXiv:1006.3255](https://arxiv.org/abs/1006.3255)
 Giacintucci S., Vrtilek J. M., Murgia M., Raychaudhury S., O'Sullivan E. J., Venturi T., David L. P., Mazzotta P., Clarke T. E., Athreya R. M., 2008, *ApJ*, 682, 186
 Gitti M., O'Sullivan E., Giacintucci S., David L. P., Vrtilek J., Raychaudhury S., Nulsen P. E. J., 2010, *ApJ*, 714, 758
 Grevesse N., Sauval A. J., 1998, *Space Sci. Rev.*, 85, 161
 Hicks A. K., Mushotzky R., Donahue M., 2010, *ApJ*, 719, 1844
 Kaastra J. S., Bykov A. M., Werner N., 2009, *A&A*, 503, 373
 Kalberla P. M. W., Burton W. B., Hartmann D., Arnal E. M., Bajaja E., Morras R., Pöppel W. G. L., 2005, *A&A*, 440, 775
 Kirkpatrick C. C., Gitti M., Cavagnolo K. W., McNamara B. R., David L. P., Nulsen P. E. J., Wise M. W., 2009, *ApJ*, 707, L69
 Koranyi D. M., Geller M. J., 2002, *AJ*, 123, 100
 Kuntz K. D., Snowden S. L., 2000, *ApJ*, 543, 195
 Markevitch M., Vikhlinin A., Mazzotta P., 2001, *ApJ*, 562, L153
 Mazzotta P., Giacintucci S., 2008, *ApJ*, 675, L9
 McNamara B. R., Nulsen P. E. J., 2007, *ARA&A*, 45, 117
 Mittal R., Hudson D. S., Reiprich T. H., Clarke T., 2009, *A&A*, 501, 835
 Nomoto K., Iwamoto K., Nakasato N., Thielemann F. K., Brachwitz F., Tsujimoto T., Kubo Y., Kishimoto N., 1997, *Nucl. Phys. A*, 621, 467
 Nulsen P., Kraft R., Stark D., Cen A Chandra VLP Collaboration 2010, in *Bulletin of the American Astronomical Society Vol. 41 of Bulletin of the American Astronomical Society, Impact of Stellar Mass Loss on the Jet of Centaurus A*. pp 657+
 O'Dea C. P., Baum S. A., Privo G., Noel-Storr J., Quillen A. C., Zufelt N., Park J., Edge A., Russell H., Fabian A. C., Donahue M., Sarazin C. L., McNamara B., Bregman J. N., Egami E., 2008, *ApJ*, 681, 1035
 O'Sullivan E., Giacintucci S., David L. P., Vrtilek J. M., Raychaudhury S., 2010, *MNRAS*, pp 868, paper I.
 O'Sullivan E., Vrtilek J. M., Harris D. E., Ponman T. J., 2007, *ApJ*, 658, 299
 O'Sullivan E., Vrtilek J. M., Kempner J. C., David L. P., Houck J. C., 2005, *MNRAS*, 357, 1134, OS05
 Peterson J. R., Fabian A. C., 2006, *Phys. Rep.*, 427, 1
 Pipino A., Kaviraj S., Bildfell C., Babul A., Hoekstra H., Silk J., 2009, *MNRAS*, 395, 462
 Rasia E., Mazzotta P., Bourdin H., Borgani S., Tornatore L., Ettori S., Dolag K., Moscardini L., 2008, *ApJ*, 674, 728
 Rasmussen J., Ponman T. J., 2007, *MNRAS*, 380, 1554
 Rasmussen J., Ponman T. J., 2009, *MNRAS*, 399, 239
 Rebusco P., Churazov E., Böhringer H., Forman W., 2005, *MNRAS*, 359, 1041
 Rebusco P., Churazov E., Böhringer H., Forman W., 2006, *MNRAS*, 372, 1840
 Roediger E., Brüggén M., Rebusco P., Böhringer H., Churazov E., 2007, *MNRAS*, 375, 15
 Salomé P., Combes F., 2003, *A&A*, 412, 657
 Sanders J. S., Fabian A. C., Allen S. W., Schmidt R. W., 2004, *MNRAS*, 349, 952
 Schombert J. M., 1987, *ApJS*, 64, 643
 Simionescu A., Werner N., Böhringer H., Kaastra J. S., Finoguenov A., Brüggén M., Nulsen P. E. J., 2009, *A&A*, 493, 409
 Simionescu A., Werner N., Finoguenov A., Böhringer H.,

- Brüggen M., 2008, *A&A*, 482, 97
- Simionescu A., Werner N., Forman W. R., Miller E. D., Takei Y., Böhringer H., Churazov E., Nulsen P. E. J., 2010, *MNRAS*, 405, 91
- Snowden S. L., Collier M. R., Kuntz K. D., 2004, *ApJ*, 610, 1182
- Vikhlinin A., Markevitch M., Murray S. S., Jones C., Forman W., Van Speybroeck L., 2005, *ApJ*, 628, 655
- Weisskopf M. C., Brinkman B., Canizares C., Garmire G., Murray S., Van Speybroeck L. P., 2002, *PASP*, 114, 1
- Werner N., Durret F., Ohashi T., Schindler S., Wiersma R. P. C., 2008, *Space Science Reviews*, 134, 337
- Xiang F., Rudometkin E., Churazov E., Forman W., Böhringer H., 2009, *MNRAS*, 398, 575